Magnetic Resonance in Medicine 51:1292–1296 (2004)

Magnetic Resonance Electrical Impedance Tomography at 3 Tesla Field Strength

Suk H. Oh,[1] Byung I. Lee,[2] Tae S. Park,[1] Soo Y. Lee,[1*] Eung J. Woo,[2] Min H. Cho,[1] Jin K. Seo,[3] and Ohin Kwon[4]

Magnetic resonance electrical impedance tomography (MREIT) is a recently developed imaging technique that combines MRI and electrical impedance tomography (EIT). In MREIT, cross-sectional electrical conductivity images are reconstructed from the internal magnetic field density data produced inside an electrically conducting object when an electrical current is injected into the object. In this work we present the results of electrical conductivity imaging experiments, and performance evaluations of MREIT in terms of noise characteristics and spatial resolution. The MREIT experiment was performed with a 3.0 Tesla MRI system on a phantom with an inhomogeneous conductivity distribution. We reconstructed the conductivity images in a 128 × 128 matrix format by applying the harmonic B_z algorithm to the *z*-component of the internal magnetic field density data. Since the harmonic B_z algorithm uses only a single component of the internal magnetic field data, it was not necessary to rotate the object in the MRI scan. The root mean squared (RMS) errors of the reconstructed images were between 11% and 35% when the injection current was 24 mA. Magn Reson Med 51:1292–1296, 2004. © 2004 Wiley-Liss, Inc.

Key words: electrical conductivity imaging; MREIT; harmonic B_z algorithm; recessed electrodes; MRCDI

Information about electrical conductivity distribution inside biological tissues is useful for many purposes, such as modeling tissues to investigate action potential propagations, estimating therapeutic current distribution during electrical stimulation, and monitoring physiological functions (1–3). In combinatory studies of functional MRI (fMRI) with other brain mapping modalities, such as EEG and MEG brain mapping, information about conductivity distribution inside the brain is essential for the precise localization of activated regions (4,6). Electrical impedance tomography (EIT) is a conductivity imaging modality in which many surface electrodes are attached to an object to measure the electric potentials produced by injection currents. However, EIT has many drawbacks, including a limited amount of measured data, low sensitivity of the surface voltage to conductivity changes at the region far from the electrodes, and the ill-posedness of the corresponding inverse problem involved in image reconstruction. Recently, a combination of MRI and EIT (MREIT) was introduced as a new conductivity imaging modality (7–9). With MREIT, one can transform the ill-posed conductivity image reconstruction problem into a well-posed one by incorporating the internal data of magnetic flux density distributions measured by an MRI scanner. In previous MREIT experimental studies (10–12), the biggest problems were object rotations inside the magnet to acquire the three components of the internal magnetic field data, and low SNR of reconstructed images. However, new MREIT reconstruction algorithms were recently introduced, along with phantom imaging results obtained without any object rotations (13–15).

In this work we present some results of MREIT phantom imaging experiments performed with the harmonic B_z algorithm and a 3.0 Tesla MRI system. After briefly introducing the fundamental principle of the conductivity image reconstruction algorithm, we present the experimental results of the conductivity imaging performance evaluation.

MATERIALS AND METHODS

Conductivity Image Reconstruction Problem in MREIT

We assume a 3D electrically conducting object. Four electrodes are attached to the surface of the object, and two currents are then injected between two chosen pairs of electrodes. For example, I_1 is the injection current between a pair of electrodes facing each other, and I_2 is the injection current between the other pair. Then the voltages V_1 and V_2 inside the object due to the corresponding DC injection currents I_1 and I_2 satisfy the following partial differential equation:

$$\begin{cases} \nabla \cdot (\sigma(\mathbf{r})\nabla V_i(\mathbf{r})) = 0 & \text{inside the object} \quad \text{for i = 1 and 2} \\ -\sigma\nabla V_i \cdot \mathbf{n} = g_i & \text{on the surface} \end{cases} \qquad [1]$$

where σ is the conductivity distribution inside the object, $\mathbf{r}$ is a position vector, $\mathbf{n}$ is the unit outward normal vector on the surface boundary, and g_i is the normal component of the current density due to the injection current I_i. The current density $\mathbf{J}_i$ inside the object is

$$\mathbf{J}_i(\mathbf{r}) = -\sigma(\mathbf{r})\nabla V_i(\mathbf{r}) \quad \text{for } i = 1 \text{ and } 2\,. \qquad [2]$$

From Ampere's law, the induced magnetic flux density $\mathbf{B}_i$ is related to $\mathbf{J}_i$ as

[1]Graduate School of East-West Medical Sciences, Kyung Hee University, Kyungki, Korea.

[2]College of Electronics and Information, Kyung Hee University, Kyungki, Korea

[3]Department of Mathematics, Yonsei University, Seoul, Korea.

[4]Department of Mathematics, Konkuk University, Seoul, Korea.

Grant sponsor: Korea Science and Engineering Foundation; Grant number: R11-2002-103.

*Correspondence to: Soo Yeol Lee, Ph.D., Graduate School of East-West Medical Sciences, Kyung Hee University, 1 Seochun, Kiheung, Yongin, Kyungki 449-701, Korea. E-mail: sylee01@khu.ac.kr

Received 5 November 2003; revised 19 January 2004; accepted 20 January 2004.

DOI 10.1002/mrm.20091
Published online in Wiley InterScience (www.interscience.wiley.com).

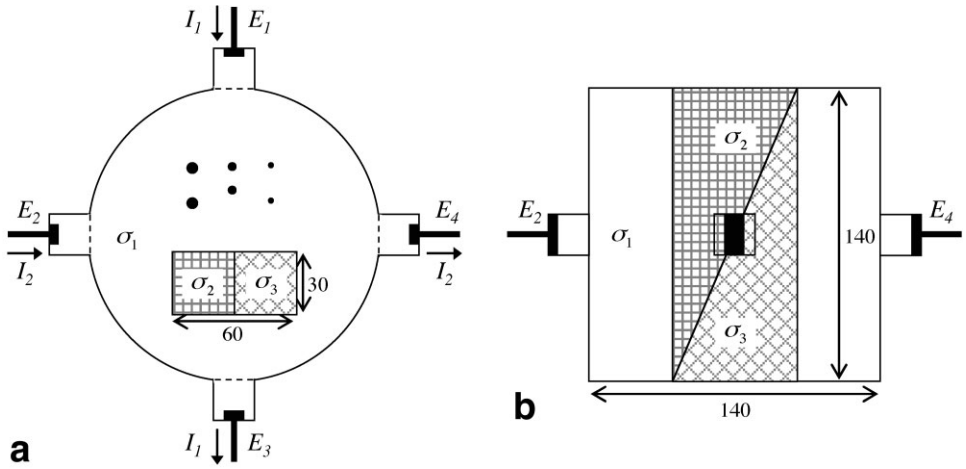

FIG. 1. (**a**) Top and (**b**) side views of the conductivity phantom. σ_1 is the conductivity of the electrolyte solution in the phantom. The σ_2 and σ_3 region consists of two sponge wedges with different physical densities. The six dots above the sponge region are cotton threads (diameter = 4 mm (left), 3 mm (middle), and 2 mm (right)). Four recessed electrodes are attached on the middle of the cylindrical surface to inject electrical currents into the phantom.

$$\mathbf{J}_i(\mathbf{r}) = \frac{1}{\mu_0}\nabla \times \mathbf{B}_i(\mathbf{r}) \quad \text{for } i = 1 \text{ and } 2\,, \qquad [3]$$

where μ_o is the magnetic permeability of the free space.

In MREIT, we measure the induced magnetic flux density using an MRI scanner and try to reconstruct images of the conductivity distribution σ using the relations in Eqs. [1]–[3]. When the main magnetic field of the MRI scanner points to the z-direction, we can obtain images of B_z^i that is the z-component of $\mathbf{B}_i = (B_x^i, B_y^i, B_z^i)$. A conductivity image reconstruction algorithm (called the harmonic B_z algorithm) was recently proposed, which uses the following key identity (13,14):

$$\frac{1}{\mu_0}\left(\frac{\partial^2}{\partial x^2} + \frac{\partial^2}{\partial y^2} + \frac{\partial^2}{\partial z^2}\right) B_z^i = \frac{\partial \sigma}{\partial x}\frac{\partial V_i}{\partial y} - \frac{\partial \sigma}{\partial y}\frac{\partial V_i}{\partial x}$$

$$\text{for } i = 1 \text{ and } 2\,. \qquad [4]$$

This is an iterative algorithm that starts with an arbitrary initial conductivity distribution σ_m with $m = 0$. In the mth iteration with $m \geq 1$, we numerically solve Eq. [1] by replacing σ with σ_{m-1} to compute V_i for $i = 1$ and 2. Plugging the measured data B_z^i and the computed V_i into Eq. [4], we can calculate $\nabla\sigma_m = \left(\frac{\partial \sigma_m}{\partial x}, \frac{\partial \sigma_m}{\partial y}\right)$. The layer potential technique is then used to obtain σ_m from $\nabla\sigma_m$. With Eq. [4], we can reconstruct a 2D conductivity image using the B_z data measured at multiple slices, including the slice of interest. Further developments of 3D conductivity reconstruction algorithms will be considered in our future studies. The harmonic B_z algorithm used in this work is described in detail in Ref. 14.

Experiments

To evaluate the performance of conductivity imaging with the harmonic B_z algorithm, we constructed a conductivity phantom (shown in Fig. 1) with a cylindrical shape (diameter and height = 14 cm). The phantom was filled with an electrolyte solution with conductivity σ_1 of 0.63 S/m (3.125g/l NaCl, 2g/l $CuSO_4$). In the middle of the cylindrical surface, four recessed electrodes were attached, and currents (I_1 and I_2) were injected into the phantom. Each recessed electrode consisted of a tube filled with low-conductivity material and a metal electrode attached on the far side of the tube. The use of recessed electrodes avoids many of the problems caused by conventional metal electrodes, such as MRI signal void around the metal electrodes due to RF signal blocking, and nonuniform current density at the interface between the metal electrodes and the phantom surface (16). The recessed electrodes were also filled with the electrolyte solution and connected with a current-driving circuitry. The recessed electrodes were $2 \times 2 \times 3$ cm^3, and the metal plate (copper) was 1 cm $\times$ 2 cm. Inside the phantom, we placed two wedge-shaped sponges facing other with no gaps in between. The sponges differed in physical density, hence the two sponges had different conductivities when they were soaked in the solution. When the two sponges were completely soaked, the conductivities of the sponges (σ_2 and σ_3) were determined to be 0.16 S/m and 0.25S/m, respectively, by means of an impedance analyzer (4192A, Hewlett Packard). To evaluate the spatial resolution of the conductivity imaging, we placed six cotton threads (2–4 mm in diameter) in parallel from the top to the bottom of the phantom. Because of some technical difficulties, we did not measure the conductivity values of the cotton threads. We assume that the threads have lower conductivity than the sponges because the threads have a higher physical density compared to the sponges.

To measure the internal magnetic field components (B_z^1 and B_z^2), we used an MR current density imaging (MRCDI) pulse sequence with a multislice flow-compensated spin-echo imaging technique (17,18). For the MRCDI pulse sequence, we applied a bipolar current pulse with current-driving circuitry. Since the current-driving circuitry was operated in a constant-current mode, the amount of injection current was kept constant despite some irregularity in the charge exchanges between the metal plates and the electrolyte solution. The pulse width of the bipolar current was set to 48 ms in all of the experiments. With two independent MRCDI scans, we measured two internal magnetic fields (B_z^1 and B_z^2) produced by currents I_1 and I_2 (Fig. 1a). During the current injection, we measured the voltage between the two electrodes, which was used in the conductivity image reconstruction.

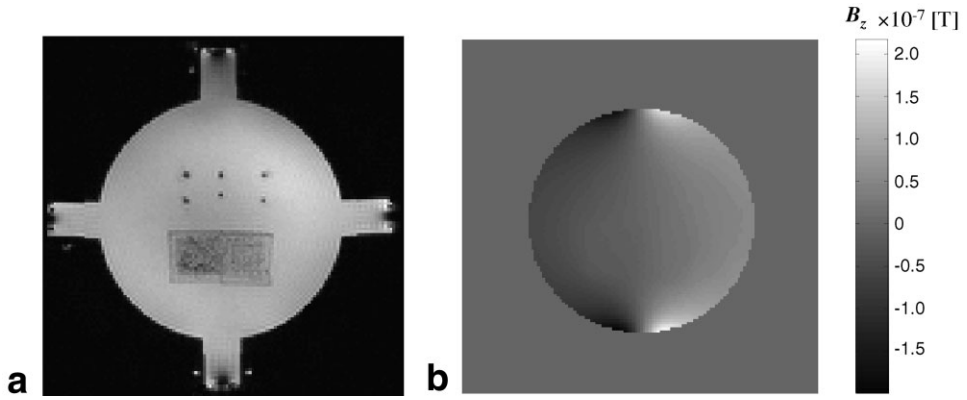

FIG. 2. **a:** Magnitude image of the conductivity phantom obtained with I_1 = 24 mA. **b:** B_z image corresponding to the left image. In the conductivity image reconstruction, only the B_z data in the circular phantom region are considered.

We performed the MRCDI scans with a 3.0 Tesla MRI system (Magnum 3.0; Medinus Inc., Korea), and acquired the MRI signals using a birdcage RF coil (diameter = 30 cm). The repetition time (TR) and echo time (TE) were 1400 ms and 60 ms, respectively. The slice thickness was 5 mm with no slice gaps. We applied the oversampling technique in both the readout and phase-encoding directions to reduce truncation artifacts in phase images. Phase images (matrix size = 128 × 128) were calculated from the *k*-space data (matrix = 256 × 256). The total MRCDI scan time to measure the two internal magnetic fields was about 12 min. To unwrap the phase images, we used Goldstein's branch-cut algorithm (19). We converted the phase images into magnetic flux density images by the use of appropriate scaling.

RESULTS

Figure 2 shows a typical magnitude image of the conductivity phantom and the corresponding B_z image obtained with the 3.0 Tesla MRI scanner. The image was obtained with the current I_1 (from electrodes E_1–E_3) of 24 mA. In Fig. 2a, we can see that the recessed electrodes are quite useful for obtaining artifact-free images inside the cylindrical region of the phantom. We obtained the B_z image in Fig. 2b from the corresponding phase image by using the phase unwrapping algorithm and appropriate scaling. Inside the circular region in Fig. 2b, the B_z values range from −155 nT to 155 nT. Since we need to measure only B_z in MREIT with the harmonic B_z algorithm, we did not apply the object-

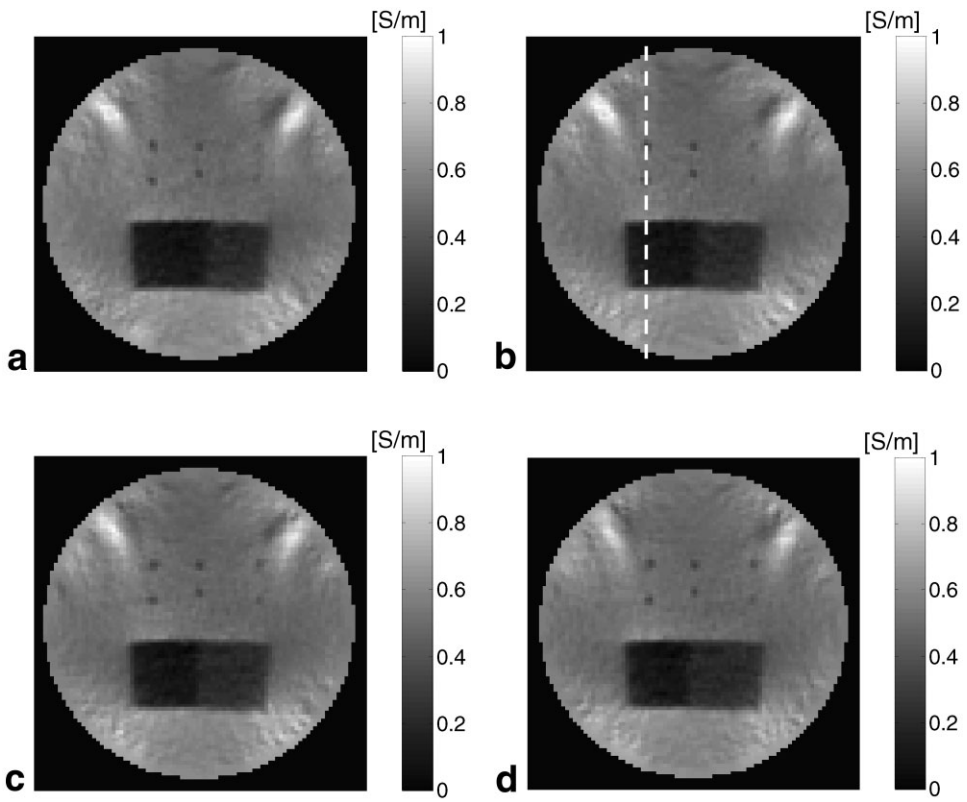

FIG. 3. Conductivity images reconstructed from the B_z data of $I_1 = I_2$ = 24 mA. Images **a–d** display the slices in a sequential order from the top to the bottom of the phantom. Slice thickness = 5 mm.

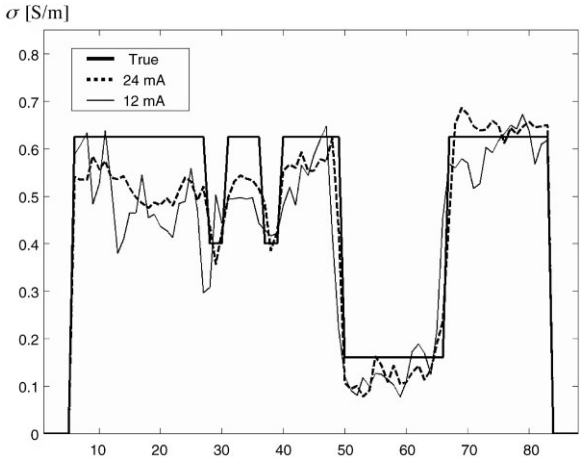

FIG. 4. Profiles of the conductivity images along the dashed lines in Fig. 3.

rotation-related geometrical error corrections during image reconstruction (10).

By applying the harmonic B_z algorithm to a set of measured multislice B_z images with 24 mA injection current and 5-mm slice thickness, we reconstructed conductivity images of the phantom (shown in Fig. 3). For the conductivity imaging, two MRCDI pulse sequences (one with I_1 = 24 mA, and one with I_2 = 24 mA) were applied consecutively. In the conductivity images, all of the cotton threads are clearly resolved. This suggests that the conductivity imaging has a spatial resolution of <2 mm when it is applied to high-contrast material imaging. Regarding the contrast-to-noise behavior, we can observe that there is good contrast between the two sponges, as well as between the sponges and the background region. From the conductivities of the sponges and the solution (0.16 S/m, 0.25 S/m, and 0.63 S/m), we can infer that a contrast of <36% can be differentiated with the conductivity imaging with an injection current of 24 mA. The four consecutive conductivity images with no slice gaps (Fig. 3a–d) show the varying size of the wedge-shaped sponges in the slice direction, demonstrating the slice-resolving power of the conductivity imaging. Figure 4 shows vertical profiles of the reconstructed conductivity images along the dashed line in Fig. 3. We found that the root mean squared (RMS) errors were 11%, 35%, and 16% at the σ_1, σ_2, and σ_3 regions, respectively, when the injection current was 24 mA. However, the errors increased to 18%, 38%, and 20% when the injection current was reduced to 12 mA. The rather large errors in the σ_2 region are due to poor SNR of the magnitude images in the region.

DISCUSSION

Since second-order differentiations of B_z provide spatial information of the conductivity distribution, the harmonic B_z algorithm can differentiate conductivity contrasts very effectively. Compared to previous results obtained with a 0.3 Tesla MRI scanner (14), the conductivity images presented here are significantly improved—mainly due to the much better SNR of the 3.0 Tesla MRI scanner. However, the harmonic B_z algorithm is weak against the random noise in measured B_z data, since numerical differentiations tend to amplify the noise. We are now devising different algorithms that require a single or no numerical differentiation.

Figure 3 shows bright spot artifacts in the peripheral regions between the electrodes where the two currents are almost collinear and their densities are very low. One can reduce these artifacts by using more than four electrodes evenly spaced around the object. The electrical safety guideline at the low-frequency range is specified as 100 mA/m^2 (20). Considering the cross-sectional area at the middle of the phantom, this guideline implies that the amount of injection current should not exceed 1.96 mA. Therefore, the noise performance should be further improved before conductivity imaging can be used in practice. For better noise performance, the SNR of B_z images should be improved first. High-SNR MRI techniques, such as fast spin echo (FSE) or gradient echo (GE) imaging sequences, will be considered in future studies. In addition to high-SNR B_z image acquisition, we are now developing effective denoising techniques based on underlying physical principles, such as $\nabla \cdot \mathbf{J} = 0$ and $\nabla \cdot \mathbf{B} = 0$. The current version of the harmonic B_z algorithm is based on the assumption of isotropic conductivity. Since many kinds of tissues have anisotropic conductivity (21), future studies should also take into account the anisotrophy of tissues.

CONCLUSIONS

We reconstructed conductivity images in a 128 × 128 matrix format by applying the harmonic B_z algorithm to the *z*-component of the internal magnetic field density data. Since the harmonic B_z algorithm uses only a single component of the internal magnetic field data, it was not necessary to rotate the object in the MRI scan. The RMS errors of the reconstructed images were between 11% and 35% when the injection current was 24 mA. The present work only shows the feasibility of MREIT as a new medical imaging modality. Considering the rapid progress that is being made in MREIT research, we expect that low-spatial-resolution conductivity imaging will applicable to animal studies in the near future.

REFERENCES

1. Sersa I, Beravs K, Dodd NJF, Zhao S, Miklavcic D, Demsar F. Electric current density imaging of mice tumors. Magn Reson Med 1997;37: 404–409.
2. Beravs K, Frangez R, Gerkis AN, Demsar F. Radiofrequency current density imaging of kainite-evoked depolarization. Magn Reson Med 1999;42:136–140.
3. Khang HS, Oh SH, Han BH, Lee SY, Cho MH, Woo EJ. A preliminary study on temperature change monitoring using the MR current density imaging technique. Meas Sci Technol 2002;12:N42–N46.
4. Baysal U, Haueisen J. Estimating tissue resistivity distribution by using in vivo EEG and MEG data. In: Proceedings of the 13th International Conference on Biomagnetism, Jena, 2002. p 682.
5. Lazeyras F, Zimine I, Blanke O, Perrig SH, Seeck M. Functional MRI with simultaneous EEG recording: feasibility and application to motor and visual activation. J Magn Reson Imaging 2001;13:943–948.
6. Liu AK, Dale AM, Belliveau JW. Monte Carlo simulation studies of EEG and MEG localization accuracy. Hum Brain Mapp 2002;16:47–62.

7. Woo EJ, Lee SY, Mun CW. Impedance tomography using internal current density distribution measured by nuclear magnetic resonance. In: Proceedings of the Annual Conference of SPIE, San Diego, 1994. Vol. 2299. p 377.
8. Ider YZ, Birgul O. Use of the magnetic field generated by the internal distribution of injected currents for electrical impedance tomography (MR-EIT). Elektrik 1998;6:215–225.
9. Kwon O, Woo EJ, Yoon JR, Seo JK. Magnetic resonance electrical impedance tomography (MREIT): simulation study of J-substitution algorithm. IEEE Trans Biomed Eng 2002;49:160–167.
10. Khang HS, Lee BI, Oh SH, Woo EJ, Lee SY, Cho MH, Kwon O, Yoon JR, Seo JK. J-substitution algorithm in magnetic resonance electrical impedance tomography (MREIT): phantom experiments for static resistivity images. IEEE Trans Med Imaging 2002;21:695–702.
11. Oh SH, Han JY, Lee SY, Cho MH, Lee BI, Woo EJ. Electrical conductivity imaging by magnetic resonance electrical impedance tomography (MREIT). Magn Reson Med 2003;50:875–878.
12. Lee BI, Oh SH, Woo EJ, Lee SY, Cho MH, Kwon O, Seo JK, Baek WS. Static resistivity image of cubic saline phantom in magnetic resonance electrical impedance tomography. Physiol Meas 2003;24:579–589.
13. Seo JK, Yoon JR, Woo EJ, Kwon O. Reconstruction of conductivity and current density images using only one component of magnetic field measurements. IEEE Trans Biomed Eng 2003;50:1121–1124.
14. Oh SH, Lee BI, Woo EJ, Lee SY, Cho MH, Kwon O, Seo JK. Conductivity and current density image reconstruction using harmonic B_z algorithm in magnetic resonance electrical impedance tomography. Phys Med Biol 2003;48:3101–3116.
15. Birgul O, Eyuboglu EM, Ider YZ. Experimental results for 2D magnetic resonance electrical impedance tomography (MR-EIT) using magnetic flux density in one direction. Phys Med Biol 2003;48:3485–3504.
16. Lee BI, Oh SH, Woo EJ, Lee SY, Cho MH, Kwon O, Seo JK, Lee JY, Baek WS. Three-dimensional forward solver and its performance analysis for magnetic resonance electrical impedance tomography using recessed electrodes. Phys Med Biol 2003;48:1971–1986.
17. Scott GC, Joy MLG, Armstrong RL, Henkelman RM. Measurement of nonuniform current density by magnetic resonance. IEEE Trans Med Imaging 1991;10:362–374.
18. Scott GC, Joy MLG, Armstrong RL, Henkelman RM. Sensitivity of magnetic-resonance current-density imaging. J Magn Reson 1992;97:235–254.
19. Ghiglia DC, Pritt MD. Two dimensional phase unwrapping: theory, algorithms and software. New York: Wiley Interscience; 1998.
20. Reilly JP. Standards and rationale in applied bioelectricity. New York: Springer-Verlag; 1998.
21. Tuch DS, Wedeen VJ, Dale AM, George JS, Belliveau JW. Conductivity tensor mapping of the human brain using diffusion tensor MRI. Proc Natl Acad Sci USA 2001;98:11697–11701.